Sensors & Transducers, Vol. 243, Issue 4, August 2020, pp. 6-23

www.sensorsportal.com

Sensors & Transducers

Published by IFSA Publishing, S. L., 2020
http://www.sensorsportal.com

Topological Superconductive and Memristive Nanostructured Toroidal-Tower Array Device System Enabled Cooper-Pairs Reentry Between States for Sensing Multiple Biomarkers

[1*] E. T. Chen, [2] J. T. Thornton and [3] S-H. Duh

[1] Advanced Biomimetic Sensors, Inc., 6710A Rockledge Drive, Suite 400, Bethesda, MD 20817, USA
[2] Bruker Nano, 19 Fortune Dr., Billerica, MA 01821, USA
[3] University of Maryland Medical System, 22 South Greene St, Baltimore, MD 21201, USA
Tel.: 240-706-5687, fax: 240-630-4051
[*] E-mail: llenchen@nanobiomimeticsensors.com

Received: 2 July 2019 /Accepted: 3 August 2020 /Published: 11 August 2020

Abstract: Topological superconductive and memristive nanostructured toroidal-tower array device systems are reported for direct electrochemical sensing of multiple biomarkers based on the biomimetic glucose…pyruvate…acetyl CoA (ACoA) fuel energy pathway of a mitochondria cell. The device comprises flexible fractional Josephson junctions (FFJJ) made of innate matrix metalloproteinase (MMP)-2 cross-linked with conductive polymers forming a first layer membrane on the electrode surface, a medium comprising of glucose and acetyl CoA (ACoA) molecules (as the GA medium), serves as an insulator or a conductor when pyruvate molecules activated the medium, and the second layer comprising of an innate Heat Shock Protein (HSP) cross-linked with the similar polymers on top of the first layer. Cooper-pairs reentry between the state of superconductivity at room temperature and the memristive state are enabled through a molecular "Valve" GA medium activated by a biomarker to switch the electron move in a 3D horizontal-vertical pathway from low Josephson frequency to high Josephson frequency, enabled the device to direct sensitive and quantitative sensing multiple-biomarkers without antibody or labeling, wherein potential applications are discussed.

Keywords: Protein–Protein Interaction Network Sensor (PPINS), Double-layer Superlattice Membrane, Multiple-Biomarker, Quantum Conductance, Flexible Fractional Josephson junction, Friedel-oscillation, 3D Cooper-pair Switch

1. Introduction

Biomarkers identified for screening diseases such as diabetes, Alzheimer's, breast cancer, lung and prostate cancer, cardiomyocytes, urinary tract infection, and pneumonia are usually associated with multiple protein-protein interactions (PPI), formed networks because research revealed over 80% proteins do not operate alone but in complexes [1-4].

Christopher Overall's group reported matrix metalloproteinase (MMP) has a significant role in the PPI network associated with several diseases [3]. For example, diabetes' hyperglycemia can activate MMP-2 concentration in the mitochondrial cell, and decreases the Heat Shock Protein (HSP) 60's concentration, which leads to disturbing the mitochondrial gap membrane potential, causes mitochondria cell dysfunction. Therefore, protein

MMP-2 networks with HSP60 in the presence of biomarker hyperglycemia contributes to myocardial dysfunction was reported [3, 5].

MMP is a family of zinc-dependent endopeptidases. The enzymes play a key role in human health for promoting newborn growth, nervous system growth, as well as in promoting various human diseases, such as cancer invasion, osteoarthritis, tissue destruction, diabetes, coronary malfunction, epilepsy and Alzheimer's [6-9]. MMP's major role is to degrade the extracellular matrix as a double-edged sword, as well as a biomarker to network intracellular with HSP60 and HSP70. The protein MMP-2 has been identified as a critical biomarker for diagnosing, monitoring and predicting multiple types of human diseases [9-14]. HSP's major roles as molecular chaperons to help refold stressed proteins also acted as immunomodulates whose capability is to transform the anti-inflammatory property when the HSP concentrations are low to the pro-inflammatory property when HSP concentrations are high [15-16].

Our group's prior work demonstrated the biomarker ATP molecules were able to be stabilized in the Tris buffer with modified cyclodextrin (CD) media promoted a long-range Direct Electron-transfer (DET) favorable status led ATP molecules directly communicate in an activated 3D-cage biomimetic MMP-2 with an HSP60-like tall cylinder membrane fabricated by a direct deposition method without cysteine, that stimulated superconductivity at the gamma frequency 60 Hz over a range from 400 aM to 2 mM without causing any extracellular ATP hydrolysis using the human milk compared with the organic milk samples [17-18]. Upon that experiences, a hypothesis was drafted, that was to fabricate an innate MMP-2/HSP60 network protein device with similar components of cross-linked polymers, to study the system DET current flow pattern for direct sensing multiple biomarkers, such as glucose and pyruvate under different concentrations without using antibodies. Further understanding of the PPI pattern in a quantitative and contour map fashion may reveal critical information between the membrane structure and the DET relay trend. If possible, we would like to predict the system may or may not have superconductivity or memristive, or lucky to possess both characteristics. Therefore, this system may pave a road for direct sensing clinically useful biomarkers without burdensome protocols.

2. Results and Discussions

2.1. The Friedel-oscillation in the Superlattice Membranes

Friedel-oscillation is a phenomenon of long-range indirect interactions between electrons on a superlattice surface [19]. Evaluations of the Friedel-oscillation were conducted based on the AFM images. Fig. 1A revealed the Friedel- oscillation in 3D AFM image with an electronic cloud surrounded on the zinc atoms of the toroidal array (200-300 nm diameter pore size) superlattice in the cross-linked innate MMP-2 polymer membrane in the 1.0 mm^2 area. Fig 1B depicts an AFM image in high sensor mode at 8.9 mm × 8.9 mm larger area showing multiple toroidal shaped structures with diameters varied from 1.8 mm to 4.8 mm and the toroidal thickness varied between 50-90 nm. The brightest spots are zinc atoms in the innate protein MMP-2 molecules, and the Friedel-oscillation was observed surrounding the zinc atom indicating the Cooper-pair electrons oscillation with the possible zinc migrations observed because the only zinc atoms came from the MMP-2 protein, there were no zinc ions in our organic cross-linked polymers. Zinc atoms serve as the flexible Josephson junction barriers connection between the superconducting polymers. Images from Fig. 1A and 1B are membranes fabricated by cross-linked triacetyl-ß-cyclodextrin (TCD), polyethylene glycol diglycidyl ether (PEG), poly(4-vinyl pyridine) (PVP) and innate MMP-2 protein as the bottom layer. The top layer was fabricated by a properly mixed solution of Heat Shock Protein (HSP60) with TCD, PEG, and PVP on the top of the MMP-2 self-assembled membrane formed a multiple-layer superlattice membrane for creating a Josephson junction superconducting qubit device. Fig. 2A depicts an AFM image of the multiple-enzyme network membrane (30 × 30 mm^2) with multiple-cluster high tower structure having the tower diameters between 500 nm to 2.4 mm, and the towers' height is about 500 nm. The strong Friedel- oscillation from Cooper-pair electron cloud due to the MMP-2...HSP60 networking alignment was observed. The MMP-2's "wedding ring" structure cavity may have 5-10 % alignment with the cylinder structured HSP60, hence formed the unique structure for promoting Cooper-pairs moving from a horizontal 2D surface direction and jumping along a vertical direction of the tower, like industry chimney discharging "electric cloud" from the nano-sized "Tesla towers" observed. In the 2D ground surface, we observed many MMP-2 formed toroidal rings with some of them have zinc atoms on top. Fig. 2B depicts such a perfect "wedding ring" with a diamond sparkling showing the Friedel - oscillation that happened on the toroidal ring filled superlattice flat surface. The thickness in the Z direction is about 70 nm. This observation was similar to the image of Fig. 1B made by MMP-2 cross-linked polymer. Fig. 2C depicts an AFM image of the same membrane in a small area of 907.9 nm x 907.9 nm of a diameter 300-360 nm toroidal ring comprising of layered many atoms with a cavity in 20-26 nm depth, and the film thickness is 11.9 nm. Fig. 2D depicts an AFM image of a perfect donut-shape toroidal qubit with an eternal pore diameter of 180-200 nm having an outside diameter of 700 nm and a thickness of 60 nm was observed. Fig. 2E depicts a 2D AFM image with multiple toroidal rings on the superlattice membrane with some of them having Josephson junction zinc atoms on the rings showing the Friedel-oscillation at

the horizontal direction, plus, several vertically oriented "Tesla tower" having strong Friedel-oscillation demonstrated the Cooper-pair electron indeed being guided along the towers, and rising vertically discharges the "cloud" of superconducting current in oscillation. The observation of the Friedel-oscillation in the membrane superlattice was a confirmation of the Cooper-pairs' hopping-flip existence [19]. More detailed 3D AFM was depicted in Fig. 2F in 30 × 30 (mm^2) having a tower density of per 45 mm^2 has one tower, hence the device may have 680-700 multiple-protein network formed Josephson "Switch tower" in switch of the direction from the Cooper-pair horizontally moving to a vertical moving along in the wall of the tower. This unique nanostructure SAM membrane with the "two-way" Friedel-Oscillation of Cooper-pair may find utility in multiple- analyte analysis and quantum energy storage and computing.

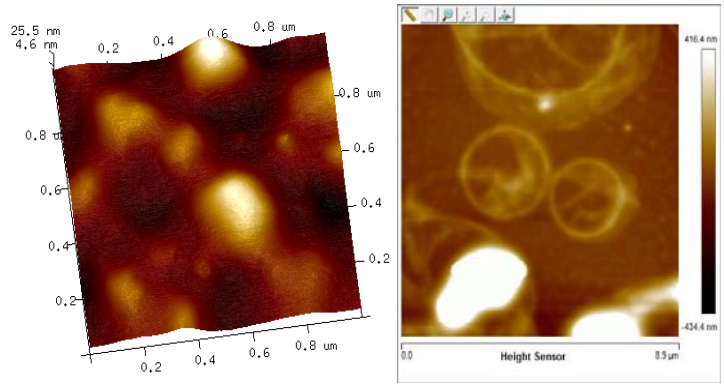

(a) (b)

Fig. 1. (a): 3D AFM image of the MMP-2 membrane as the first layer in 1.0 μm^2; (b): 2D AFM image in a larger area.

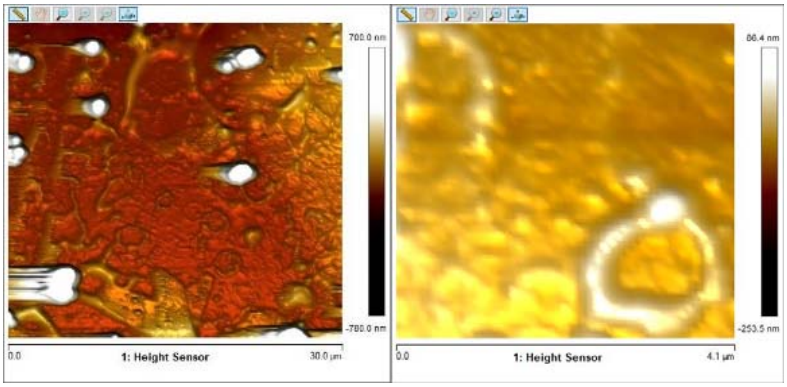

(a) (b)

Fig. 2. (a). Second layer of tower structure HSP60 AFM image multiple-enzyme network membrane (30 × 30 μm^2) which is on top of the first layer of MMP-2.
Fig. 2 (b). Toroidal "diamond ring" structure in detail.

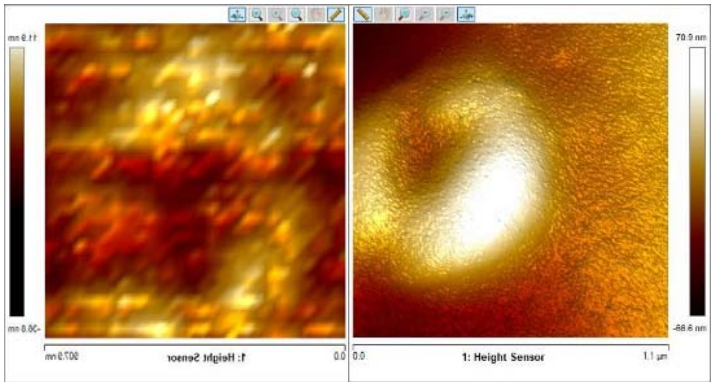

(c) (d)

Fig. 2 (c). 907.9 nm × 907.9 nm area and a diameter 300-360 nm toroidal ring in detail;
Fig. 2 (d). Donut-shape toroidal qubit.

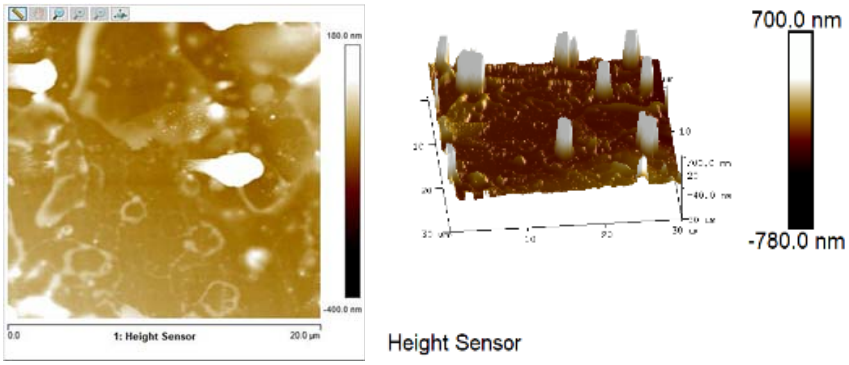

(e) (f)

Fig. 2 (e). Another AFM image from a different area for the tower glow with Cooper-pair moving compared with the background superlattice of toroidal rings.
Fig. 2 (f). 3D AFM image of the nanometer size "Tesla Tower".

2.2. The Proposed Model Used for Evaluation of the Innate HSP60/MMP-2 Superconductive/ Memristive Device

2.2.1. An Engineering Working Art Model for the HSP60/MMP-2 Device

A proposed working model used for the illustration of the HSP60/MMP-2 device is presented in Fig. 3A. The left side of Fig. 3A shows the 3D HSP60/MMP-2 membrane comprises of a nano-toroidal structure for the first layer membrane formed on the surface of the electrode by innate MMP-2/PEG/PVP/TCD, and the second layer is in the alignment of the MMP-2 toroidal array cavities, comprised of HSP60/PEG/PVP/TCD; the top is a poreless cap.

The right side of Fig. 3A shows the working model in multiple PPI network between proteins HSP60 and MMP-2, and also the possible PPI between the "Zinc Finger" of MMP-2 and COO- group of TCD and pyridine group of PVP, to form a biomimetic hiding glucose oxidase (GOx) to attract glucose; the "Zinc Finger" of MMP-2 of Cys_1His_3, TCD, PEG, and PVP may interact with acetyl CoA (ACoA), then the electron-transfer between the glucose, ACoA and the receptors may form an insulator-like "platform" to guide the move direction of Cooper-pair, which is moving along the edge of the HSP60 wall; here the "insulator" is not tangible, rather its function is to switch current direction; the efforts may well form a hiding biomimetic pyruvate dehydrogenase (PDH), hence to attract pyruvate at a low frequency [20-28]. Many research reports and review articles were published in the area of PPI network mapping [3, 29-30], but very few, if any, study the local and long-range Cooper-pair DET chain movement in low frequency and its oscillation at high frequency among multiple proteins and multiple biomarkers in a superconductive or a memristive fashion with flexible Josephson junctions. The results obtained from our experiments may reveal interesting characteristics regarding the PPI/multiple biomarkers' sensing/energy storage and quantum computing information.

Fig. 3B depicts the symbol of the flexible Josephson toroidal vortex junction. The center "8" shape hummingbird is a symbolic representation of the circular electron-relay system.

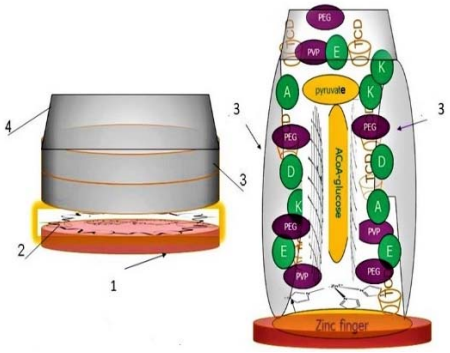

Fig. 3 (a). HSP60/MMP-2 model used for elucidating the proposed protein MMP-2... HSP60 PPI in the form of DET chain in the toroidal...cylinder membrane through a GA medium insulator platform. "1": the electrode; "2": MMP-2 cross-linked first layer membrane; "3": HSP60 dimer Cross-linked second layer membrane; "4": the PEG…PVP…TCD cross-linked cap.

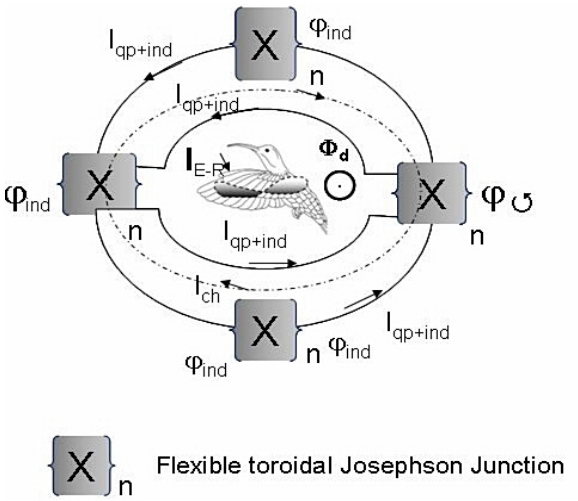

Fig. 3 (b). Model of Flexible toroidal Josephson junction. Obtained a permission from E. T. Chen et al. [35].

2.3. Accessing the Superconductivity and Mem-element Characteristics

2.3.1. Quantum Conductivity

The hallmarks of the JJ characteristics are (1) at a DC voltage = 0,

$$I_s = I_c \sin(\triangle\varphi), \quad (1)$$

where I_s is the supercurrent, I_c is critical current, $\triangle\varphi$ is the phase difference between the waves of two superconductors appears at the DC Josephson junction; (2) at a finite DC voltage, the phase change of the superconducting wave vs. time caused oscillation at the AC Josephson Junction is proportional to $2eV_{DC,}$ i.e. [31-32]:

$$\partial\varphi/\partial t = (2e/h)V_{DC,} \quad (2)$$

where φ is the phase difference between the waves of two superconductors appears at two sides of the Josephson barrier, V_{DC} is the potential difference across the barrier, and h is the Plank constant ($1.055x10^{-34}$ Js), e is the electron charge.

Fig. 4A depicts the i-V curve profiles of the HSP60/MMP-2 network protein device in 10 mM PBS pH 7.0 buffer with a changing scan rate from 20 Hz to 25 kHz at room temperature. Among the curves, 20 kHz and 25 kHz have also shown 10 consecutive scan cycles for comparison. There is no hysteresis event observed, but Josephson junction's vortex inductivity was observed from Ej /Ec =1 (Ej is the Josephson energy, and Ec is the capacitive energy) at 60 Hz, to Ej /Ec > 1 [33-34] as the scan rate increase to 25 kHz, indicating the phase change induced Josephson energy increased more than the increase of the capacitance energy at zero-bias at room temperature and without a microwave magnetic power applied to the system. Quantum qubit's superposition states were seen between state "1" at v =0, Is > 0; state "0" at v=0, Is=0; state "-1" at v=0, Is<0 from 60 Hz, 2 kHz, 20 kHz and 25 kHz. Phase change was also observed. The curve at 60 Hz shows a reversible pair of direct electron-transfer (DET) peaks with the highest amplitude located at zero-bias, indicates a fractional Josephson junction presents, and the Cooper-pair moves in the superlattice structures (toroidal rings predominantly contributing on the surface over the vertical tall tower does) have eternal electron relay of the receptors at a low frequency than at higher frequency; verse versa, at a higher frequency, the Cooper-pairs have stronger oscillation through the tall tower structure with the 20-50-fold higher superconducting current than that of the DET at low frequency. We call this phenomenon "Cooper-pair's Snowboarding". There was no memristive hysteresis behavior observed among the scan rates.

Fig. 4B (R) shows the glucose in 60 μg/dL concentration brings a perfect memristive hysteresis loop curve with a $2x10^5$-fold increased the signal intensity compared with the control in Fig. 4A (L) at 60 Hz. Fig. 4C further shows the DET_{red} peak current at -0.616V increased exponentially when the consecutive scan cycles increased to 10 and the time elapsed 503.6 s with a first-order rate constant 0.0044 $\mu A.s^{-1}$. This is an evidence of an embedded biomimetic glucose oxidase enzymatic activity happened in the membrane cavity, even though there was no such enzyme was fabricated in the membrane. It demonstrates the multiple-layer membrane promoted receptors DET relay caused this event. It was also noticed the hypoglycemia glucose eliminated all superconductivity at higher frequency compared with the control curves in Fig. 4A.

The memristive peaks in Fig. 4D are observed at scan rate 20 and 60 Hz, and the current increased 10^6- 10^7-fold compared with the PBS control samples at 60 Hz in Fig. 4A, that indicates ACoA also direct bio-communicates with the biomimetic choline acetyltransferase (ChAT) receptors of the membrane of the sensor. Comparison of the i-V curves of the DET peaks at 20 and 60 Hz between glucose and ACoA in Fig 4B and 4D, respectively. The intensity of the 3 nM ACoA peak is several orders of magnitude higher than that of the glucose 3.33 μM (60 μg/dL), that indicates the nature of the membrane contains biomimetic ChAT or biomimetic pyruvate dehydrogenase complex (PDC) enzymatic complexation, and the Guest-Host inclusion strength might be much higher than biomimetic glucose oxidase at 20 and 60 Hz. Fig. 4E depicts i-V curves under the impact of 10 μM choline in the PBS buffer over the scan rate from 60 Hz to 25 kHz. The flat i-V curves at 60 Hz for 10 scan cycles demonstrate choline turned the original control i-V curve at 60 Hz at a fractional Josephson junction superconductive state at zero-bias shown in Fig. 4A to a topological resistance state. Choline alone shows no memristive characteristic compared with that of glucose in Fig. 4B and ACoA in Fig. 4D at 60 Hz, that indicates ACoA is

in the determination enzymatic step toward ChAT than that of choline [35], however we observed the i-V curves with choline turned "on" the Josephson superconducting oscillation at higher scan rate at 2 kHz, 20 kHz and 25 kHz, respectively.

Fig. 4F (L) shows the hysteresis point of the memristive curves at zero-bias and with zero current at scan rate 20 and 60 Hz with 5 fM pyruvate, and the peak intensity at -750 mV is 2×10^7-fold increased at 60 Hz compared with the PBS control sample in the Fig. 4A, that indicates the biomarker pyruvate is a good candidate to promote a long-range electron-relay at low frequency and it may help to accomplish a Josephson oscillation at high frequency if there is a PPI effect with other biomarkers. The i-V curve at 20 kHz, there are 2 DET_{ox} peaks observed, which is very special and meaningful for its ability of complexing with the biomimetic PDH receptors in the sensor membrane. Fig. 4G (R) depicts the molecular-biomarker formed medium platform as a key component of a topological switch "Valve" with topological resistance shown under different scan frequencies over 60 Hz to 25 kHz in the i-V curves of the GA medium, which comprises of 3 nM ACoA and 1 mg/dL glucose in the PBS solution. Among the curves, 10 consecutive cycles are shown in 60 Hz and 20 kHz, respectively. Glucose concentration impacts on the GA medium's i-V curves was displayed in two scan rates, 60 Hz and 20 kHz, respectively, 1 mg/dL is for the curve "a", 80 mg/dL is for the curve "b" and 300 mg/dL is for the curve "c", while kept the ACoA concentration constant in 3 nM, respectively. The results demonstrate the glucose concentration change did not impact the intensity of the i-V curves, because the i-V curves are superposition at 60 Hz and 20 kHz, respectively among the different glucose concentration levels over the hypoglycemia, the normal and the hyperglycemia level. The GA medium indeed acted as a topological insulator.

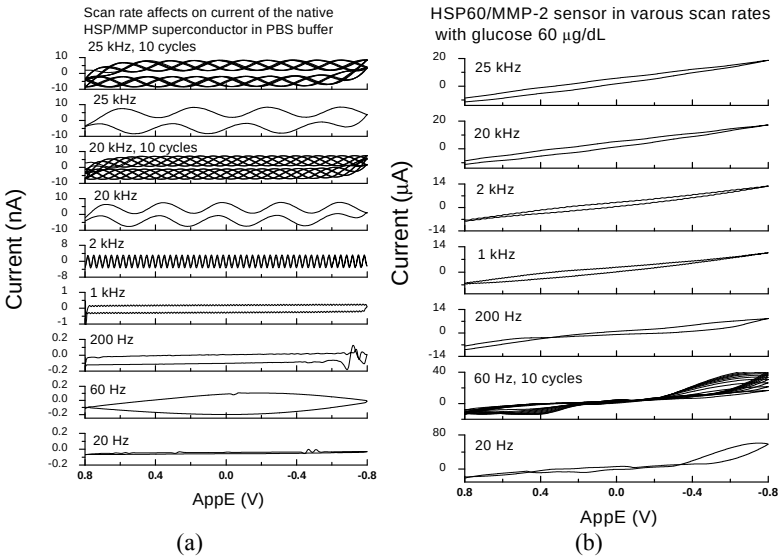

Fig. 4 (a). Scan rate impacts on the i-V curves of the HSP/MMP device over 20 Hz to 25 kHz in pH 7.0, 10 mM PBS buffer solutions. **Fig. 4 (b).** 60 µg/dL(3.6 µM) glucose effects the i-V curves when scan rate changes from 20 Hz to 25 kHz in the PBS buffer.

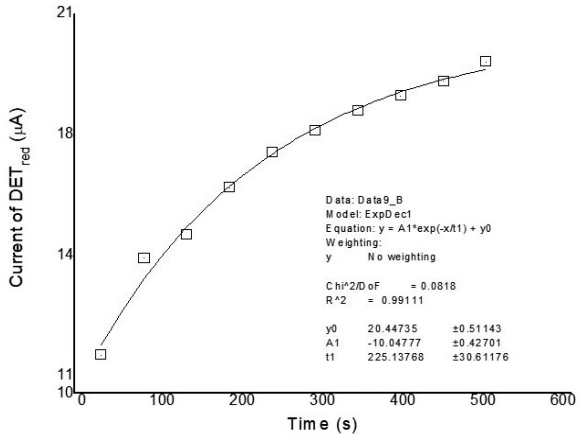

Fig. 4(c). DET_{red} current at -0.616 V vs. time of 10 scan cycles in the presence of 60 µg/dL glucose at san rate 60 Hz in the PBS buffer according to Fig. 4 (b).

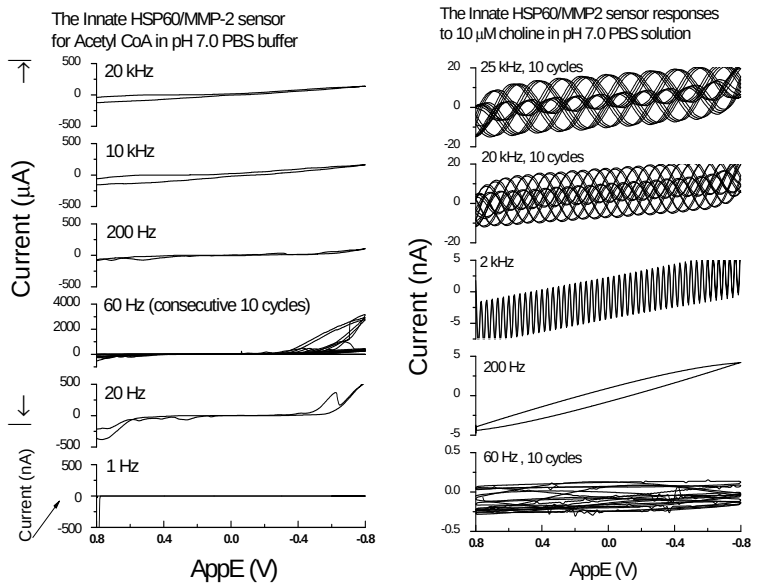

(d) (e)

Fig. 4 (d). Scan rate impacts on the i-V curves of 3 nM ACoA in the PBS buffer. At 60Hz, it has 10 scan cycles.
Fig. 4 (e). i-V curves impacted by 10 μM choline from 60 Hz to 25 kHz. At higher scan rate over 2 kHz to 25 kHz, superconductive curves at zero-bias are shown with phase change and Crosspoint nodes and superposition activities, that indicate the strong Cooper-pair oscillation having an infinite circular resonates, while keep absolute signal strength constant without energy lose. At 200 Hz, its state is the memcapacitive included the origin in the loop.

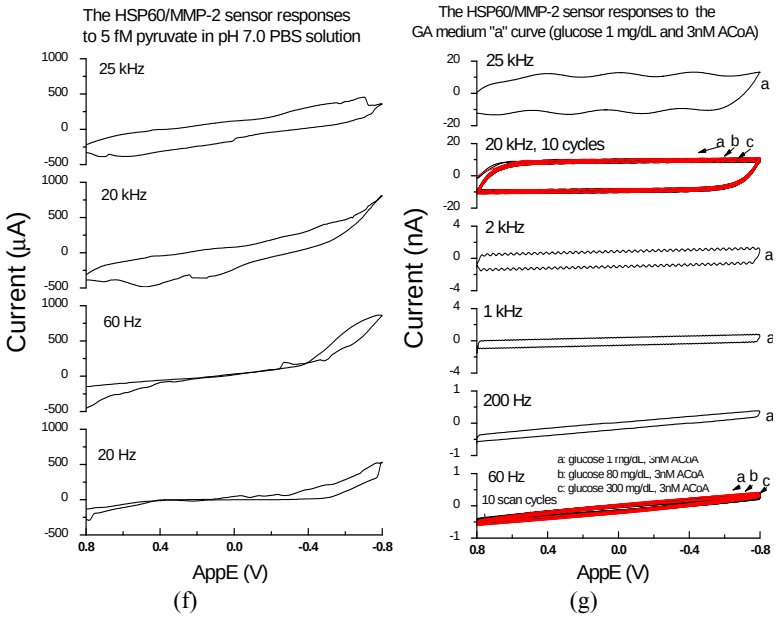

(f) (g)

Fig. 4 (f). i-V curves of 5 fM pyruvate impacted by the scan rate from 20 Hz to 25 kHz. **Fig. 4 (g).** i-V curves of various glucose concentrations impact on the i-V curves of the GA medium at difference scan rates.

2.3.2. Accessing the Quantum Conductance of the Device in the PBS buffer

Fig. 5 shows the curves of quantum conductance vs. potential from 60 Hz (Panel A), 2 kHz (Panel B), 20 kHz (Panel C) and 25 kHz (Panel D) at ± 1 Δ (± 1.0 mV), at room temperature under the condition of without an external magnetic field applied. The intensity of the quantum conductance increases as the scan rate increase from 60 to 20 kHz, after that, the reduced intensity at 25 kHz was observed. Fig. 6 depicts the linear relationship between Josephson frequency and the Shapiro Step Voltage, which the slope gives KJ value is that of 241.8, which is equal to 483.5979/2 from a 2π Josephson periodicity to a 4π Josephson periodicity of the FFTJJ vortex [36-38].

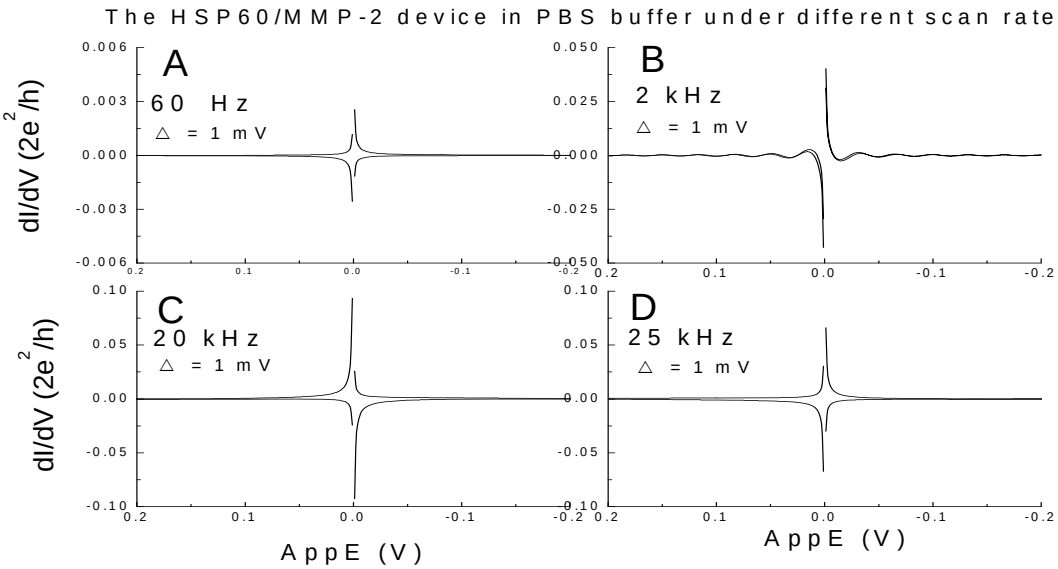

Fig. 5. Quantum conductance of the HSP60/MMP-2 device vs. potential at 60 Hz, 2 kHz, 20 kHz and 25 kHz, respectively.

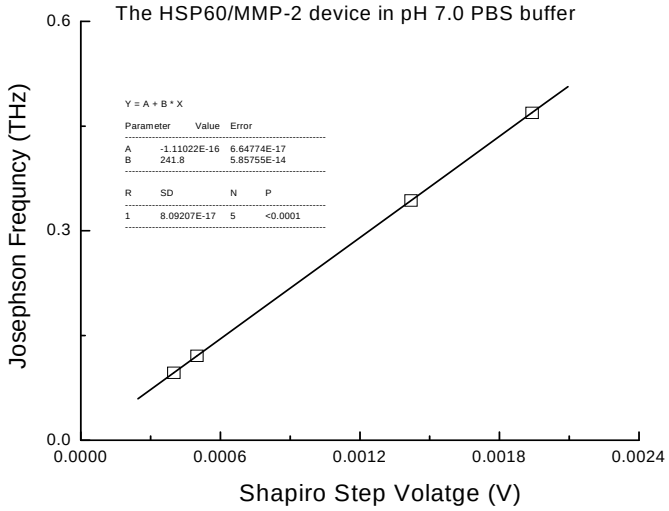

Fig. 6. Plot of Josephson frequency vs. Shapiro step voltage over scan rate 60 Hz to 25 kHz.

2.3.3. The Memristor

Memristor is a semiconductor whose resistance varies as a function of flux and charge. This allows it to "remember" what has passed through the circuit [39-42]. G({x},t) which is state dependent

$$I(t) = G(\{x\},V, t)\, V(t) \qquad (3)$$

From Fig. 4A's i-V curves there is no hysteresis point observed, and no memristive was observed. However, significant memristive characteristics were observed under the impact of biomarkers, such as glucose in Fig. 4B, Acetyl CoA in Fig. 4D, pyruvate in Fig. 4F were explained and demonstrated in the above section.

2.4. Sensing of Multiple Biomarkers

2.4.1. Sensing Glucose.

The conventional methods for multiple biomarker analysis have been based on multiple antibodies' sandwich ELISA methods, but the protein cross-interference has been a key roadblock hampered the analysis in burdensome time-consuming procedures and low precision. The goal of the article is to seek an approach for developing multiple biomarkers analysis possible methods without using the sandwich antibody that based on the unique superlattice structure and the Cooper-pair's capability through handing out a "tool" to the Cooper-pairs, and stimulate their uncovering potential with sensitivity for analytes and durability for energy storage.

Our attempt to choose appropriate biomarkers, such as glucose and pyruvate as our testing model analytes, was based on the unique nanostructured tall "Tesla tower" on the superlattice toroidal array of the HSP60/MMP-2 membrane. According to literature, inactivated MMP-2 molecules, there are imidazole receptors chelating with zinc ions, the coordination geometry, proton, and electron transfers and the displacement of water molecules formed the long electron-relay chain based on a favorable low ΔG [43-44]. The chaperoning system is a major component of the anti-stress mechanism in human cells, such as HSP60 molecule interacts with its co-chaperone HSP10 to form a network in mitochondria [16]. There are Ala 10, Asp 11, Glu105, Lys 109, Lys 449 and Glu462 form a complex in the human chaperonin in a 3D football shape in coordination with HSP10 for helping stressed proteins refolding [45-46]. Our cross-linked polymer TCD, PEG, and PVP associated with MMP-2 and HSP60, therefore all of these conditions encouraged us to propose that this HSP/MMP-2 network device may be able to conduct multiple analyte sensing and at the same time to produce energy if we would balance the overwhelming high-frequency oscillation from the Cooper-pairs and enhance the memristive so that the Cooper-pairs might be able to carry on two tasks: sensing multiple analytes and producing JJ superconducting storage energy. Fig. 7A depicts the device responses to various glucose concentrations covered clinically useful range from hypoglycemia, normal to hyperglycemia 10 mg/dL to 1000 mg/dL in five levels through the i-V curves of the Cyclic Voltammetric (CV) method at scan rate 60 Hz compared with the control. The curves are shown glucose several magnitudes promoted significant DET current increase as the concentration increase compared with the control that reflected in the contour plot of the glucose concentration vs. DET_{red} location and MEM peak current shown in Fig. 7B. We also see the mem peak current increased.

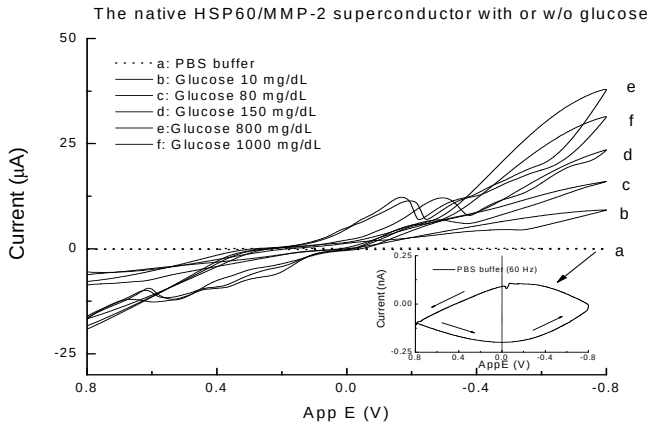

Fig. 7(a). Device responses to various glucose concentrations from hypoglycemia to hyperglycemia 10 mg/dL to 1000 mg/dL in the i-V curves at a scan rate 60 Hz compared with the control.

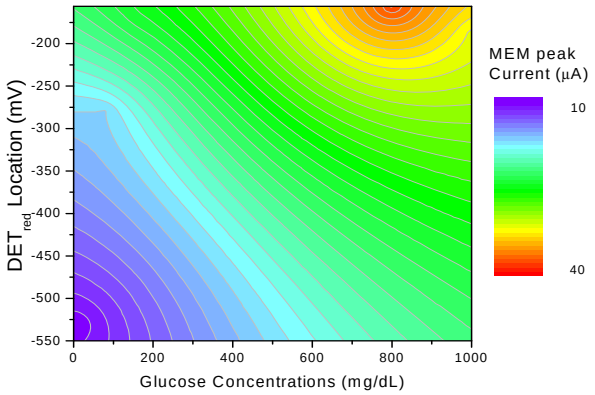

Fig. 7 (b). Contour map between the MEM peak current, DET peak location and the glucose concentrations based on data shown in Fig. 7 (a).

2.4.2. Comparing the Sensitivity

Comparing the sensitivity of glucose detection among the three types of peaks: the memristive peak, DET_{red} and DET_{ox} peaks, results shown DET_{red} peak current has no trend observed, but DET_{ox} current shows a sensitivity of 0.0044 μA/(mg.(dL)$^{-1}$) from 80 to 1.0 g/dL, and the MEM peak has a sensitivity of 0.0039

μA/(mg.(dL)$^{-1}$) from 10 to 800 mg/dL, that indicates DET_{ox} peak is more sensitive at higher concentration than that of the Memristive peak, but MEM peak is more sensitive at lower end concentration as shown in Fig. 7C. The insert is for the DET_{ox} peak current vs. glucose concentration.

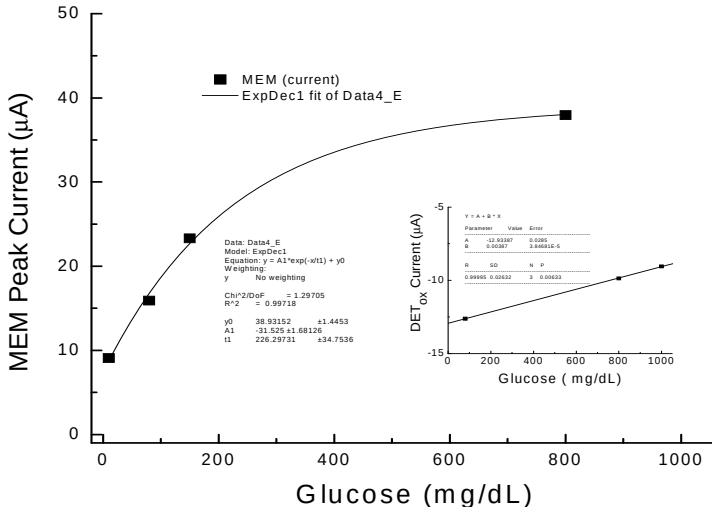

Fig. 7 (c). Calibration curve of memristive current vs. glucose concentrations. The insert is the calibration of the DET_{ox} current vs. glucose concentrations in the PBS buffer.

2.4.3. Sensing Pyruvate

2.4.3.1. The Glucose...ACoA (GA) Platform Approach

The Josephson coupled-superconductor effect is inherent in many superconductor-insulator-superconductor (S-I-S) tunnel junctions if the two sides of barriers are sufficiently thin to allow the coupling energy from the Cooper pair tunneling at the coherent wave state between the two superconductors to exceed thermal fluctuations [30, 49-50]. Majorana zero modes (MZMs) in nonconventional d-wave topological superconductors (d-WTSCs), are extensively studied in recent years [31(a), 38, 51-57] because of their non-Abelian statistics [51-55] and the potential application in topological quantum computation (TQC) [27, 54-55]. Our group reported a self-powered multiple flexible toroidal vortex Josephson junction (FTVJJ) array superconductive/mem-element superlattice quantum bit (Sulqubit) device for quantum computing with non-volatile memory and non-dissipation energy storage in room temperature within one device assembly. The device comprises of multiple layer organo-metallic cross-linked polymers having various superlattice structures, which works under normal pressure without an applied external magnetic field based on a d-wave electron – relay in the membranes that initiated and promoted Cooper pairs coherently quantum transmitting and amplifying waves in changing phases within and across the FTVJJ barriers, that comprised of a d-wave topological superconductor (TSC)/a 133 μm thickness dielectric insulator/a nanopore semiconductor with superposition states at zero-bias by the Majorana fermions induced proximity was reported [27, 57]. The paramount challenge facing the multiple biomarker screening and monitoring is the requests of limited using antibody (because for some cases of pandemic diseases, such as coronary virus Covid-19, there was no antibody is available). We thought an approach of solely rely on the presence of Cooper-pair of multiple PPI induced proximity in the JJ vortexes may not enough to carry on the tasks, because the lack of an appropriate memristive from Fig. 4A was identified.

As we know, glucose-derived pyruvate is a principal source of acetyl CoA (ACoA) in all brain cells, through pyruvate dehydrogenase complex (PDC) reaction [58]. The human brain consumes 20 % of whole-body oxygen and glucose through glycolytic pathway yields pyruvate, a key precursor for ACoA, which feeds the TCA cycle, herein ACoA activities in brain mitochondria cells, which is 4 -10 times higher of ACoA than non-excitable tissues [58]. Our group reported a nanostructured biomimetic PDC sensor was capable to selectively direct detect single brain cancer cells and could mimic an "ATP Lid" based on a self-assembled membrane (SAM) comprising of mono imidazole derivative dimethyl β-cyclodextrin (mM-β-DMCD) cross-linked with TCD, PEG, PVP and o-nitrophenyl acetate [21, 22].

The major dominant driving force is the "snowboard jumping" of the Cooper-pairs' momentum, which shows a strong oscillation in Fig. 4A from 2000 Hz to 25 kHz in the buffer solutions. Fig. 3 on the right-hand side art model illustrates our approaches to overcome the problem: (1) use glucose as a "ladder" lean onto the "Tesla Tower" because above section Fig. 7A shows glucose induced DET

peaks at 60 Hz; (2) choose ACoA as a cofactor helping glucose forming a topological platform media, that Cooper-pairs may recognize the platform and "willing" to be led by the "glucose-ACoA helper" for a quantum diving down to the sensor's toroidal array surface from the platform, and demonstrate its topological behavior; (3) Finally the Glucose...Pyruvate...Acetyl CoA (G...P..A) formed a long-range electron-relay chain that promoted the Cooper-pairs either capable to be topologically quantum conductive or capable to be a memristor in remembering of the past event [34, 42, 48]. It is not surprising, this multiple analyte G...P...A chain approach, i.e., the PPI network approach, matched with the common cell energy metabolism analyte chain, it utilizes multiple enzymes for conducting hydrolysis and oxidative reactions and produce energy.

2.4.3.2. Pyruvate Activated the Valve of the GA Medium Platform

Based on the i-V curves in Fig. 8 Panel A shows the device has orders of magnitudes increased peak current in memristive characteristics in the presence of 3 nM ACoA (curve b in the PBS buffer only, 10 scan cycles) compared with the curve "a" of the GA medium having very weak peak current reflected the topological resistance increased significantly in the presence of the GA media, that indicates ACoA alone promotes activating of the PPI of HSP60, based on the hiding strong expression of the PDC enzymatic activity (the PDC may be formed by the cysteine groups of MMP-2, PEG, PVP, and TCD by hydrogen bounding and π-π interaction, or hydrophobicity interaction which enabled a topological resistance, that expels hyperglycemia's activation of MMP-2, in turn, the GA medium may suppress the potential existence of the enzymatic activity from glucose oxidase. Together the GA medium acted as a key component of an electric valve when pyruvate joined the G…P…A relay, enabled to guide Cooper pairs either go to the road as a topological quantum superconductor or go to the road as a memristor; in Panel B, the i-V curve in the presence of 80 mg/dL glucose alone shows a DET_{ox} peak intensity is 0.3 % of the intensity of curve "b" with 3 nM ACoA in the PBS buffer in Panel A. In Panel C, an i-V curve shows the second evidence of a topological resistor's behavior over 0.8 V to -0.8 V during 10 cycles of consecutive scans at 60 Hz in a GA medium comprising of 80 mg/dL glucose and 3 nM ACoA, that supports our hypothesis: the GA media platform promotes the PPI between MMP-2 and HSP60 by selectively suppress glucose's activation of MMP-2, and promotes HSP60's normal function. Quantitation of pyruvate under antibody-free and label-free conditions might be expected. In Panel D, there was no DETox peak observed with pyruvate alone, compared with the i-V curve "b" in the presence of 10 pM pyruvate with the GA media in Panel E, which shows ± 80-fold enhancing supercurrent at zero-bias at 1 kHz compared with the zero current curves "a" from the GA media in Panel E. Therefore, this HSP/MMP-2 device may be used as a model for mimicking mitochondria's energy production.

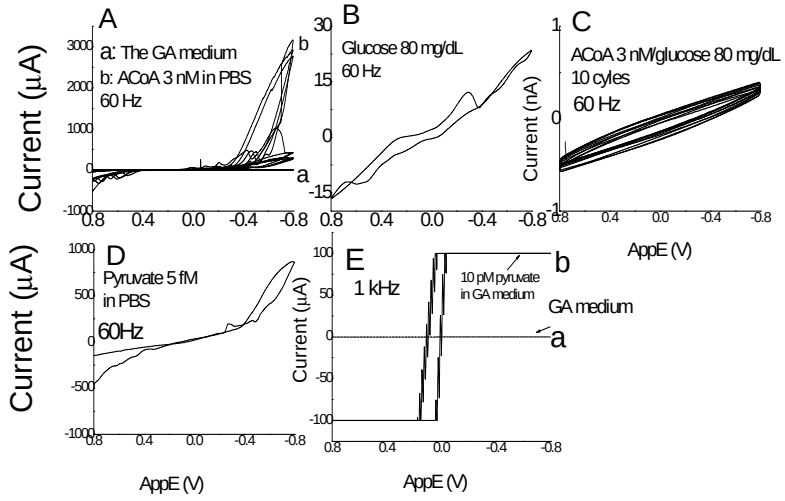

Fig. 8. Device senses various analytes at scan rate 60 Hz compared with or without the GA medium for panel A to D, 1 kHz at panel E.

Fig. 9 shows the device is capable to measure pyruvate from 5 fM, 50 fM to 10 pM, (100 pM was not shown) in the GA media solution with a 60 Hz scan rate compared with the GA control media. Panel A curve b in the presence of 5 fM pyruvate shows hysteresis characteristics of the memristor-like behavior compared with the GA control media. Panel B shows the DET current increased significantly as the pyruvate concentration increase from 50 fM to 10 pM in 10 consecutive scan cycles compared with the GA

control, and the signal was in orders-of-magnitudes increased compared with the controls. Now the Cooper-pairs demonstrated they are memristive at low 60 Hz that enabled us to conduct amperometric quantitation at a well-defined mild applied potential. Fig. 9C shows the curve of the relative signal intensity vs. phase change in the presence of 5 fM pyruvate in the GA medium at 469 GHz Josephson frequency with a signature hysteresis cross point and a 4π d-wave Josephson periodicity rather than a 2π compared with the GA media control. The success of training Cooper-pairs quantum jumping "up"- oscillating, and a "10-meter Diving" from the GA platform, that led us to believe the toroidal array JJ structure and the "Tesla mini-tower" helped Cooper-pair's two-way superconducting/memristive switch in a 3D fashion, even the original i-V curves of the PBS buffer did not show such capability, through the platform approach, Cooper-pairs' potential can be realized and demonstrated.

Fig. 9D shows the sensitivity of the tested DET_{ox} current related to pyruvate concentrations over 5 fM to 0.1 nM is 102 mA/nM, which is 1.3×10^{12} –fold sensitive than that of glucose testing. The insert in Fig. 9D is for the calibration curve of DET_{red} vs. pyruvate concentrations. Fig. 10 further shows the Cooper-pairs' capability as a memristor at 469 GHz and as a superconductor at Josephson frequencies from 97 GHz to 343 GHz with superposition at p(1, 0) and p(-1, 0) and p(0,0) state at zero-bias.

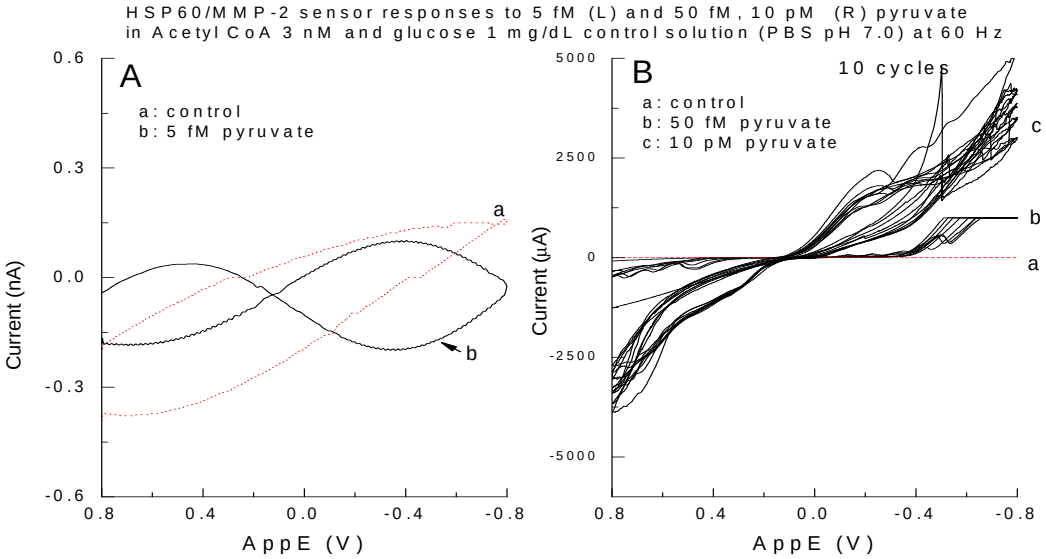

Fig. 9 (a-b). i-V curves of 5 fM (a), 50 fM and 10 pM pyruvate (b) compared with the GA media controls comprised of 3nM ACoA and 1 mg/dL glucose solutions in pH 7.0 PBS at 60 Hz scan rate.

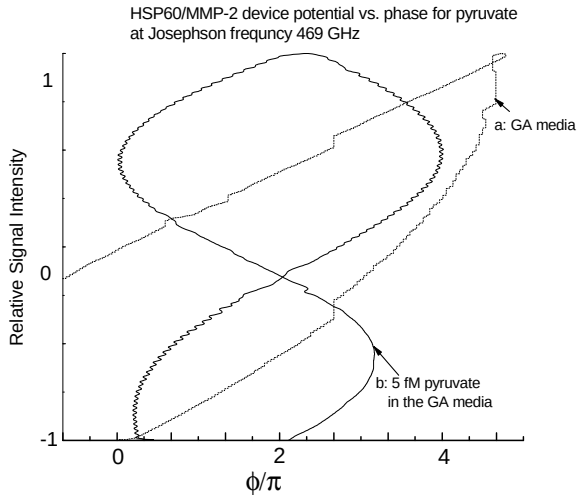

Fig. 9 (c). Fractional Josephson juction's relative signal vs. phase ϕ at 4π in the presence of 5 fM pyruvate in the GA media at Josephson frequency 469 GHz compared with the GA media control.

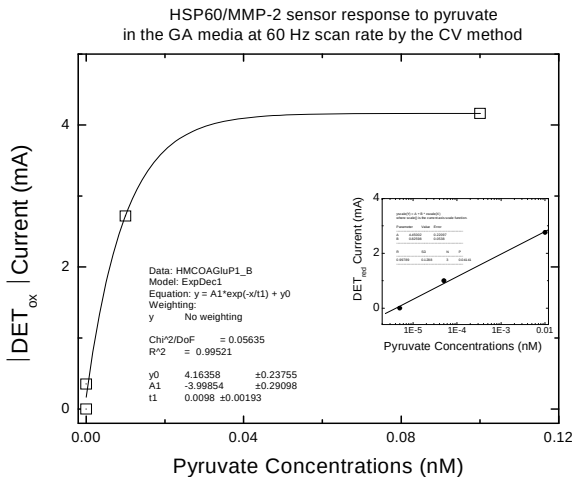

Fig. 9 (d). Calibration curve of the absolute value of the DET_{ox} peak current vs. pyruvate concentrations over 5 fM to 0.1 nM in the GA media with scan rate 60 Hz. The insert is the calibration curve of the DET_{red} peak current vs. pyruvate concentrations in a semi log plot.

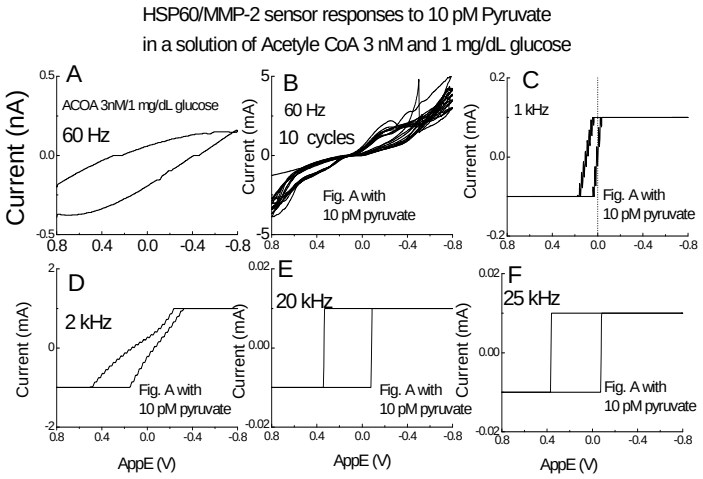

Fig. 10. Cooper-pairs capability as a memristor at Josephson frequency 469 GHz and as a superconductor at Josephson frequencies from 97 GHz to 343 GHz in the GA medium.

2.4.4. Topological Quantum Conductance Due to Pyruvate's Participation in the Majorana Zero Mode

Stern's group reported the observation of Majorana bound states of Josephson vortices in topological superconductors, and the equations of three types of energy contributions to the Josephson vortices in a long circular junction in a Sine-Gordon system was published [59]. The Josephson junction energy was from the Cooper pair, the magnetic energy was from the inductivity of the circular vortex, and the charge energy was from the SIS quantum capacitor-like device [59]. The vortex suppression of the supercurrent effect also was considered in the equation. However, there was no further analysis of how each component energy contributes to the system superconductivity from the experimental data. Cosmic's group reported seeing the vortex in a Josephson array based on a fractional Josephson Effect in the vortex lattice [60]. The Hamiltonian of the Josephson Junction Array (JJA) was given in the combinations of the first part of charging energy obtained from all arrays and the second part of the Josephson Effect energy [60]. Our group's prior work had experimentally quantified the contributions from the fractional superlattice qubit to the device's kinetic energy and the potential energy to the quantum conductance by using the 3D dynamic map method at room temperature without external magnetic field applied [38]. The modified Sine-Gordon system energy for our d-wave vortex array is:

$$E^{n}_{JJA} = (½)C^{-1}{}_{i}(Q - en_{1...i})^2 \quad (4)$$

$$E^{n}_{L} = (½)\,\mu_0 N^2_{n=1..i}.A.L^{-1}_{n=1..i}.I^2_{n=1..i}\,, \quad (5)$$

where E^{n}_{jjA} is the charge energy of Josephson Junction arrays at n = 1..i; Q is the charge, C is the total capacitance at n= 1..i, en is the n quantum particles at 1..i data point with an energy periodic in h/e for Josephson effect for d-wave [61]; E^{n}_{L} is the Inductive energy induced by the circular toroidal array. N is the turning number around the toroidal porous at n =1..i, A is the cross-sectional area of the porous, L is the length of the wending, μ_0 is the magnetic permeability constant in free space; I is current. The toroidal arrays are in series connected. Recent publication from our group regarding the FFTJJ multiple-variable study in 3D dynamic maps was presented in the literature [38]. The 3D mapping method used in this report is to show the Majorana Zero Mode (MJM) at the Fermi energy level related to the peak current, zero-bias, and the quantum conductance visually. Results from the evaluation of the pyruvate's promotion of quantum conductance at a higher frequency are further presented in a 3D dynamic map in Fig. 11A.

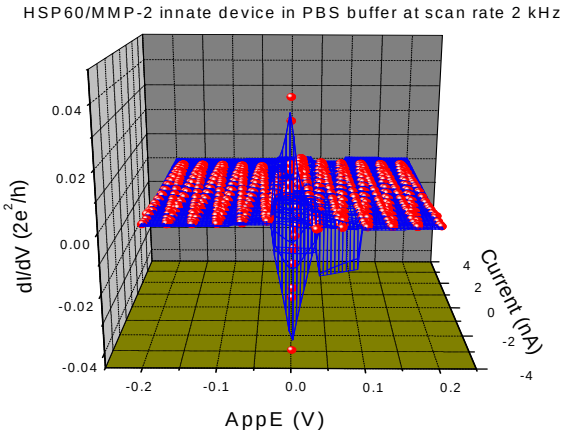

Fig. 11 (a). Quantum conductance 3d map in 2 kHz scan rate in the PBS buffer.

Fig. 11A shows there is a zero-energy Fermi surface with Cooper-pairs transmission crossing the JJ at Zero bias having the multiple states in superposition in the PBS buffer only. As a comparison, the superposition is also presented in Fig. 11B with 10 pM

pyruvate in the GA media, the quantum conductance was orders of magnitude higher (74,667-fold) than that of the control. Fig. 11C shows the superpositioning of the states in the plot curves of supercurrent vs. potential with 10 pM pyruvate in the GA medium at 97 GHz compared at 153 GHz of the Josephson frequency. Fig. 11D shows the 2D plot of the quantum conductance vs. potential at zero bias in the presence of 10 pM pyruvate at 97 GHz compared at 153 GHz of the Josephson frequency, in the GA medium.

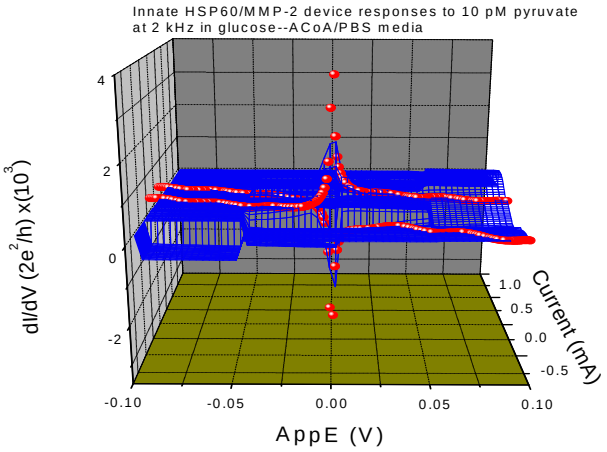

Fig. 11 (b) depicts the quantum conductance map for the HSP60/MMP-2 device in the presence of 10 pM pyruvate in the GA media solution at the same scan rate.

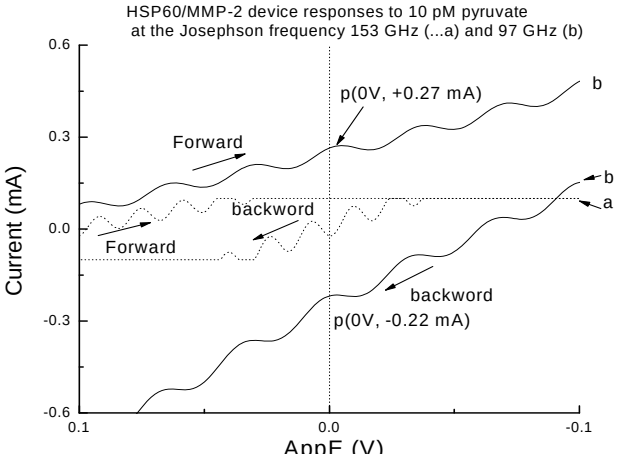

Fig. 11 (c). Superposition states at zero-bias in the presence 10 pM pyruvate in the Josephson frequency 153 GHz "a" vs. "b" at 97 GHz.

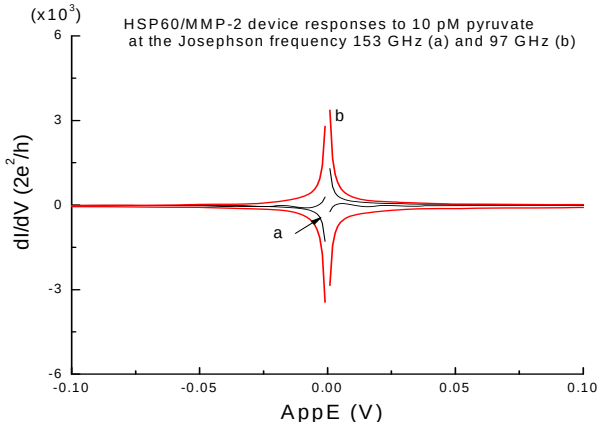

Fig. 11 (d). Plot of quantum conductance vs. potential in the presence of 10 pM pyruvate in the Josephson frequency 153 GHz curve "a" vs. 97 GHz, curve "b".

2.5. Assessing Multiple Biomarkers' Contributions to Quantum Conductance

Based on the results obtained from the i-V curves of DET_{ox} peak current of glucose alone from 80-1000 mg/dL (4.46 mM - 55.7 mM), and Pyruvate (50 fM to 100 pM) using the GA media, a contour map is presented in Fig. 12 with the Z represents the quantum conductance covers Josephson frequency from 97 GHz to 467 GHz. Fig. 12 shows the higher quantum conductance associated with 50 fM to 100 pM concentration pyruvate having an absolute values of 0.35 to 4.16 mA current of the DET_{ox} peak, while the entire glucose concentration range has a small contribution to the lowest values of conductance that indicates the GA media platform acted as the topological insulator, it leads Cooper-pairs jumping-diving in a long-range tunneling fashion along the toroidal vortex wall. Pyruvate has a wide range of concentration contributed to the higher values of quantum conductance.

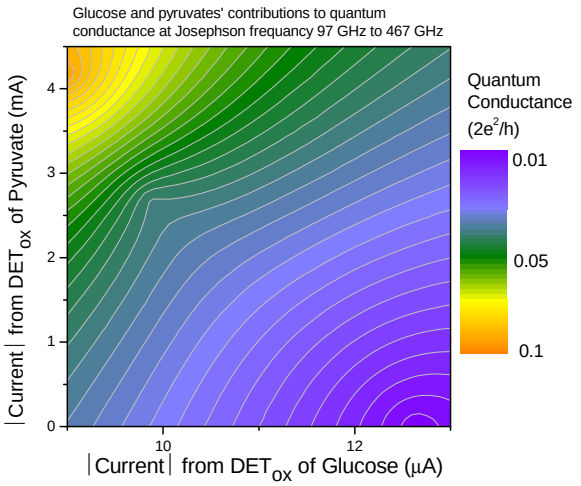

Fig. 12. Contour map of the DET_{ox} current from glucose and pyruvate contributions to the quantum conductance.

2.6. Quantitation of Pyruvate Using the Chronoamperometric Method (CA)

Based on our innovative multiple protein network approach associated with the GA medium, we were able to direct quantify pyruvate without use antibody by the CA method. Fig. 13 shows the curves of current vs. time profiles over the pyruavte concentration from 5 fM to 1 µM compared with the GA control. The inserts are the enlarged control and a curve with 5 fM pyruvate. The semi-log plot of the calibration curve was shown in Fig. 14. Fig. 14 shows the regression equation y Scale (y)= 715.0 + 154.3*log(x), n=24 (8 levels), r= 0.99, $S_{y/x}$ = 61, p<0.0001. The Detection of Limits (DOL) is 13 aM over the measured range with a Relative Pooled Standard Deviation (RPSD) value 1.4 %.

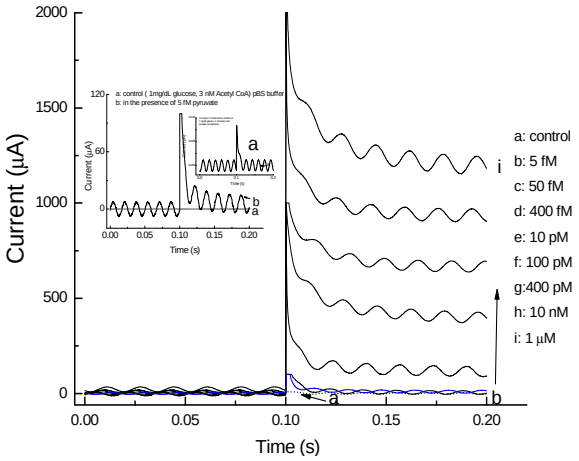

Fig. 13. Curves of current vs. time with or without pyruvate over 5 fM to 1 µM compared with the GA medium control. Each sample run triplicates.

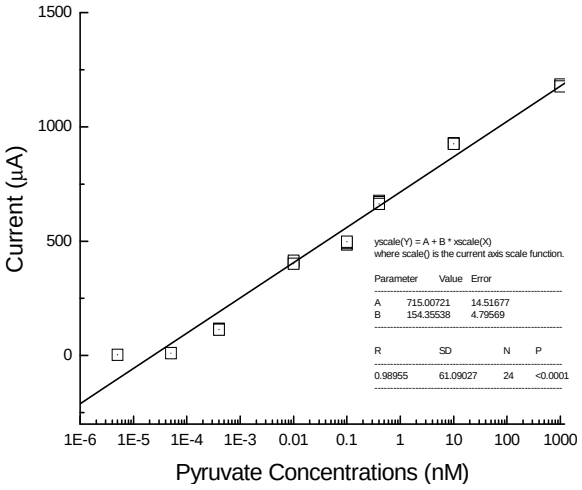

Fig. 14. Semi-log plot of the calibration curve.

3. Experimental

The innate HSP60/MMP-2 device was prepared with two steps: the first step was to form an MMP-2 polymer layer by a self-assembling method with compositions of the innate MMP-2, triacetyl-ß-cyclodextrin (TCD), polyethylene glycol diglycidyl ether (PEG) and poly (4-vinylpyridine) (PVP) with appropriate propositions deposited on the surface of gold chips at 37^0C for 96 hours after that followed the wash and dry procedures [31b]. The second layer was fabricated by mixture solutions of HSP60, PEG**,** PVP and TCD with appropriate propositions deposited on the surface of the first layer at 37^0C for 72 hrs. After that, the wash and dry procedures were followed [31b].

The GA medium was freshly prepared in the final concentration comprising of 1 mg/dL glucose and 3 nM ACoA in pH 7.0, 10 mM PBS solution (auto clayed double distilled water for cells), and further went through 0.2 µm filter filtration and degassing.

The morphology of the AU/SAM was characterized using an Atomic Force Microscope (AFM) (model Dimension Edge AFM, Bruker, MA). Data collected in TappingMode using silicon probes with a 5-10nm tip radius and ~300kHz resonance frequency (Probe mode TESPA-V2, Bruker, MA).

All electrochemical data were collected by the Epsilon voltammetry working station with the software package for various methods applications (BASi, IN), and the figure plots, and statistical analysis, curve fitting were conducted using the OriginPro software package (OriginLab, MA).

4. Conclusions

Topological superconductive and memristive nanostructured toroidal-tower array HSP60/MMP2 devices demonstrated the system with a topological GA medium has enabled Cooper-pairs reentry between states, i.e., superconductive state and memristive state in the presence of biomarkers, therefore enabled the device sensing multiple biomarkers, such as glucose, pyruvate, and ACoA under antibody-free and label-free conditions with different Josephson frequency as their finger-prints, hence this technology potentially eliminated interference. The medium acted as the topological insulator; it leads Cooper-pairs jumping-diving reentry in a long-range tunneling fashion along the toroidal vortex wall. This approach paved a foundation for further quantitative analysis of complicated PPI networks in biological specimens.

The GA medium turned the device to a superconductive state at zero-bias when 10 pM pyruvate activated the medium at Josephson frequency 97 GHz, that produced quantum conductance in 74,667-fold higher than the GA medium displayed in the 3D dynamic map showing the d-wave Cooper-pairs crossed the FFJJ in perpendicular to the Marjoram Zero-Mode (MZM) surface might provide parameters useful for researchers to study the PPI network among many known and unknown enzymes for fast screening therapeutic drugs for diseases.

Acknowledgments

E. Chen thanks Dr. Kasica's help and discussions and thanks to the NIST NanoLab for the cleanroom and other equipment.

References

[1]. F. B. Correia, E. D. Coelho, J. P. Arrais, *et al.,* Handling noise in protein interaction networks, *Hindawi, Biomed Research International,* Vol. 2019, | 2019, Art. 8984248.

[2]. V. S. Rao, K. Srinivas, G. N. Sujini *et al.,* Protein-protein interaction detection: methods and analysis, *Int. J. Proteomics*, 2014, 2014, 147648.

[3]. P. G. Jobin, G. S. Butler, C. M. Overall, New intracellular activities of matrix metalloproteinases shine in the moonlight, *BBA Molecular Cell Research*, 1864, 2017, pp. 2043-2055.

[4]. T. Zininga, L. Ramatsu and A. Shonhai, Heat shock protein as immunomodulants, *Molecules*, 23, 2018, 2846.

[5]. F. Fan, Y. Duan, F. Yang, *et al.,* Deletion of heat shock protein 60 in adult mouse cardiomyocytes perturbs mitochondrial protein homeostasis and causes heart failure, *Cell Death & Differentiation*, 27, 2020, pp. 587–600.

[6]. W. C. Parks and R. P. Mecham, Matrix metalloproteinases, *Academic Press*, San Diego, 1998.

[7]. K. Siemianowicz, W. Likus and J. Markowski, Metalloproteinases in Brain Tumors, in Molecular Considerations and Evolving Surgical Management Issues in the Treatment of Patients with a Brain Tumor (Terry Lichtor, Ed.), *IntechOpen*, 2015.

[8]. E.-M. Schnaeker, R. Ossig, T. Ludwig *et. al.,* Microtubule-dependent matrix metalloproteinases-2/ matrix metalloproteinases-9 exocytosis: Prerequisite in human melanoma cell invasion, *Cancer Research*, 2004, 64, pp. 8924-8931.

[9]. M. Rydlova, l. Holubec jr., M. Ludvikova jr, D. Klfert Biological activity and clinical implications of the matrix metalloproteinases, *Anticancer Research,* 28, 2008, pp. 1389-1398.

[10]. F. Riedel, K. Gotte, J. Schuwalb, K. Hormann, Serum levels of matrix metalloproteinase-2 and -9 in patients with head and neck squamons cell carcinoma, *Anticancer Research*, 20, 5A, 2000, pp. 3045-3049.

[11]. K. Dahiya, R. Dhankhar, Updated overview of current biomarkers in head and neck carcinoma, *World J. of Methodology*, 6, 1, 2016, pp. 77-86.

[12]. S. Ghargozlian, K. Svennevig, H-J Bangstad *et. al.,* Matrix metalloproteinases in subjects with type 1 diabetes, *BMC Clinical Pathology*, 9, 2009, Art. 7.

[13]. M. Hermandez-Guillamon, S. Mawhirt, S. Blais, *et. al.,* Sequential beta-amyloidal degradation by the matrix metalloproteinases MMP-2 and MMP-9, *J. of Biol Chem*, 290, 24, 2015, pp. 15078-15091.

[14]. R. Wang, G. Q. Zeng, R. Z. Tong, D. Zhou, Z. Hong, Serum matrix metalloproteinase-2: A potential biomarker for diagnosis of epilepsy, *Epilepsy Research,* 122, 2016, pp. 114-119.

[15]. T. Zininga, L. Ramatsui, and A. Shonhai, Heat shock proteins as immunomodulators, *Molecules,* 2018, 23, 2846.

[16]. A. A. A. Asea, N. N. A. A. Krishnan, P. Kaur (Eds.), Heat shock protein-based therapies, *Springer*, 2015.

[17]. E. T. Chen, J. T. Thornton, S-H. Duh and P. T. Kissinger, Nanobiomimetic Structured Organo-Metallic Devices Direct Rapid Real-time Monitor Atto Molarity ATP in Biological Specimens, *TechConnect Briefs in Diagnostics*, 2019, pp. 423-426. https://briefs.techconnect.org/wp-content/volumes/TCB2019/pdf/791.pdf

[18]. E. T. Chen, J. T. Thornton and S-H. Duh, 3D-Cage Structured Biomimetic MMP-2/HSP60-Like Organo-Metallic Devices Sensitively Response to ATP Concentration Change Used for Defining of Anti-inflammatory and Pro-inflammatory Status, *Sensors and Transducers*, Vol. 236, Issue 8, August 2019, pp. 28-39.

[19]. M. Ternes, M. Pivetta, F. Patthey and W-D Schneider, Creation, electronic properties, disorder, and melting of two-dimensional surface-state-mediated adatom, *Progress in Surface Science,* 85, 2010, pp. 1-27.

[20]. E. T. Chen, S-H. Duh, C. Ngatchou, J. T. Thornton and P. T. Kissinger, Selectivity study for a reagent-less and

enzyme-free nanopore glucose sensor against interferences from non-glucose sugars and other Substances, *Nanotech*, 3, 2011, pp. 101-104.

[21]. E. T. Chen, J. Thornton, C. Christelle, S-H. Duh and P. Kissinger, Nanostructured biomimetic pyruvate dehydrogenase complex (PDC) sensors selectively detect single brain cancer cell having the ability to mimic the "ATP Lid", *NSTi- Nanotech,* 2, 2013, pp. 107-110.

[22]. E. T. Chen, Nanostructured Biomimetic Sensing and Energy Storage: Organic Memristor/Memcapacitors, *Dekker Encyclopedia of Nanoscience and Nanotechnology, 3rd Edition,* January 18, 2017.

[23]. E. T. Chen, J. T. Thornton, S-H. Duh and P. T. Kissinger, Organic Nanobiomimetic Memristive/Memcapacitive Devices Ultrasensitive Direct Detect Matrix Matelloproteinase-2 in Human Serum, *Biotech, Biomaterials and Biomedical*, *TechConnect Briefs*, 2017, 271-274.

[24]. E. T. Chen J. T. Thornton and Jr. C. Mulchi, Early Forming a Hummingbird-like Hovering Neural Network Circuitry Pattern with Reentrant Spatiotemporal Energy-Sensory Orientation Privileged to Avoid "Epilepsy" Based on a Biomimetic Acetylcholinesterase Memcapacitor Prosthesis, *Sensors and Transducers,* Vol.191, Issue 8, August 2015, pp. 84-99.

[25]. E. T. Chen, Book chapter of Nanobiomimetic sensors and technology, Dekker Encyclopedia of Nanoscience and Nanotechnology, *CRC Press,* March 8, 2013.

[26]. E. T. Chen, J. T. Thornton and S-H. Duh, *3D*-Cage Structured Biomimetic MMP-2/HSP60-Like Organo-Metallic Devices Sensitively Response to ATP Concentration Change Used for Defining of Anti-inflammatory and Pro-inflammatory Status, *Sensors and Transducers,* Vol. 236, Issue 8, August 2019, pp. 28-39.

[27]. E. T. Chen, Chapter 3, Room-Temperature Self-Powered Nanostructure Organo-Metallic Superconductive Devices in Nanoengineering, Quantum Science and Nanotechnology Handbook (S. E. Lyshevski, Ed,), *CRC Press,* 2019.

[28]. J. Snider, M. Kotlyar, P. Saraon, et. al., Fundamentals of protein interaction network mapping, *Molecular System Biology*, 11, 2015, 848.

[29]. A. S. Bie, C. Comert, *et. al.,* An inventory of interactors of the human HSP60/HSP10 chaperonin in the mitochondrial matrix space, *Cell Stress and Chaperones*, 25, 2020, pp. 407–416.

[30]. E. Wolf, G. Arnold, M. Gurvitch and J. Zasadzinski (Eds.), Josephson Junctions, History, Devices, and Applications, *Pan Stanford Publishing Pte, Ltd,* 2017.

[31]. (a) E. T. Chen, J. T. Thornton, P. T. Kissinger and S.-H. Duh, Discovering of Collagen-1's Role in Producing Superconducting Current in Nanobiomimetic Superlattice Structured Organometallic Devices at Room Temperature Enabled Direct Quantitation of Sub pg/mL Collagen-1, *TechConnect Briefs, Informatics, Electronics and Microsystems,* 2018, pp. 43-46. (b). E. T. Chen, J. T. Thornton, P. T. Kissinger, S-H. Duh, Nanostructure Protein Toroidal Array Devices Promoted Room Temperature Superconductivity and Direct Sensing of Collagen-1, *Sensors and Transducers,* Vol. 228, Issue 12, December 2018, pp. 48-62.

[32]. G. Wendin, Quantum information processing with superconducting circuits: a review, *Rep. Prog. Phys.,* 80, 2017, 106001.

[33]. A. Blais, Quantum computing with superconducting Qubits (part 1), *CSSQI 2012*, https://uwaterloo.ca/institute-for-quantum-computing

[34]. J. Martinez-Rincon and YV Pershin, Bistable nonvolatile elastic-membrane memcapacitor exhibiting a chaotic behavior, *IEEE Transactions on Electron Devices,* 58, 6, 2011, pp. 1809–1812.

[35]. E. T. Chen, J. T. Thornton, P. T. Kissinger, S-H. Duh, The Advantages of human milk recognize the spatiotemporal locations of toxins and intelligently bypass them by forming a *Hummingbird-Like* hovering neural network circuitry based on an organic biomimetic c*holine acetyltransferase m*emristor/memcapacitor prosthesis, *Sensors and Transducers*, Vol. 203, Issue 8, August 2016, pp. 69-83.

[36]. http://en.wikipedia.org/fractional_vortices

[37]. F. Loder, A. P. Kampf, T. Kopp *et. al.,* Magnetic flux periodicity of h/e in superconducting loops, *Nature Physics*, 4, 2008, pp. 112-115.

[38]. E. T. Chen, J. T. Thornton, P. T. Kissinger, and S-H. Duh, Utilization of the Flexible Fractional Josephson Toroidal Arrays for Sensing, Memory Storage, and Quantum Computing, *Sensors and Transducers*, Vol. 228, Issue 12, December 2018, pp. 30-47.

[39]. J. Martinez-Rincon, MD Ventra, YV Pershin, Solid-state memcapacitive system with negative and diverging capacitance, *Physical Review B, 2010, 81(19, pp.* 195430-195437.

[40]. M. D. Pickett, G. Medeiros-Ribeiro and R. S. Williams, A scalable neuristor built with Mott memristors, *Nature Materials*, 12, 2013, pp. 114-117.

[41]. M. Suri and B. DeSalvo, Phase Change Memory and Chalcogenide Materials for Neuromorphic Applications: Emphasis on Synaptic Plasticity, in Advances in neuomorphic memristor science and applications, R. Kozma, R. E Pino, G. E. Pazienza (Eds.), Ch. 10, *Springer*, 2012, pp. 155-178.

[42]. M. D. Ventra, Y. V. Pershin, On the physical properties of memristive, memcapacitive, and meminductive systems, *Nanotechnology,* 24, 2013, 255201.

[43]. O. Kleifeld, P. E. Van den Steen, A. Frenkel et. al., Structural characterization of the catalytic active site in the latent and active natureal gelatinase B from human neutrophils, *The Journal of Biological Chem.,* 275, 44, 2000, pp. 34335-34343.

[44]. S. Nisemblat, O. Yaniv, A. Parnas, et al., Crystal structure of the human mitochodrial Chaperonin symmetrical football complex, *PNAS*, 112, 19, 2015, pp. 6044-6049.

[45]. A. L. Horwich, Molecular chaperones in cellular protein folding: the birth of a field, *Cell*, 157, 2014, pp. 285-288.

[46]. K. Rizzolo, W. A. Houry, Multiple functionalities of molecular chaperones revealed through systematic mapping of their interactionnetworks, *J Biol. Chem.*, 294, 6, 2019, pp. 2142–2150.

[47]. L. Gold, Does 40-Hz oscillation play a role in visual consciousness? *Consciousness and Congnation*, 8, 2, 1999, pp. 186-195.

[48]. E. T. Chen, J. Thornton and Jr. C. Mulchi, Nanobiomimetic Memcapacitor Memory Devices Identify Circadian Rhythm Dysfunction and Predict Early Signs of "Epilepsy" Using Reentrant Energy-Sensory Images, *Advanced Manufacturing, Electronics, and Microsystems: TechConnect Briefs*, 2015, pp. 200-203.

[49]. S. Frolov, Quantum Transport, www.sergeyfrolov.wordpress.com/teaching

[50]. S. Kivelson, Superconductivity and Quantum Mechanics at Micro – Scale, *Stanford University*. www.youtube.com/watch?v=yx666k2xH8E

[51]. Y. Fukaya, S. Tamura, K. Yada, Y. Tanaka, P. Gentile, and M. Cuoco, Inter-orbital topological superconductivity in spin-orbit coupled superconductors with inversion symmetry breaking, *Phys. Rev. B,* 97, 2018, 174522.

[52]. H-T. Kim, High-Tc mechanism through analysis of diverging effective mass for YaBa2Cu3O6+x and pairing symmetry in cuprate superconductors, *Int. J. Mod. Phys. B*, 32, 2018, 1840031, https://arxiv.org/ftp/arxiv/papers/1710/1710.07754.pdf

[53]. J. Linder, Y. Tanaka, T. Yokoyama, A. Sudbø, and N. Nagaosa, Unconventional superconductivity on a topological insulator, *Physical Review Letters,* 104, 6, February 2010, 067001.

[54]. O. A. Awoga, A. Bouhou, A. M. Black-Schaffer, Domain walls in a chiral d-wave superconductor on the honeycomb lattice, *Phys. Rev. B*, 96, 2017, 014521.

[55]. M. Kheirkhah, Z. Yan, Y. Nagai, and F. Marsiglio, First and second-order topological superconductivity and temperature-driven topological phase transitions in the extended Hubbard model with spin-orbit coupling, *Phys. Rev. Lett.,* 125, 2020, 017001.

[56]. E. T. Chen, J. T. Thornton, P. T. Kissinger, S-H. Duh, Nanostructure Protein Toroidal Array Devices Promoted Room Temperature Superconductivity and Direct Sensing of Collagen-1, *Sensors and Transducers,* Vol. 228, Issue 12, December 2018, pp. 48-62.

[57]. E. T. Chen, J. T. Thornton, S-H. Duh and P. T. Kissinger, Utilization of the Flexible Toroidal Vortex Josephson Junctions for Self-Powering 150K Superlattice Bits Having Non-volatile Memory Storage in One Device Assembly at Room Temperature, *TechConnect Briefs in Quantum Devices,* 2019, pp. 260-263.

[58]. A. Szutowicz, H. Bielarczyk, A. Jankoska-Kulawy, et. al., Acetyl-CoA the key factor for survival or death of cholinergic neurons in course of neurodegenerative diseases, *Neurochem Res,* 38, 2013, pp. 1523-1542.

[59]. E. Grosfeld, A. Stern, Observing Majorana bound states of Josephson vortices in topological superconductors, *PNAS*, 108, 29, 2011, pp. 11810-11814.

[60]. R. Cosmic, H. Ikegami, A. Lin, K. Inomata, Circuit QED-based measurement of vortex lattice order in a Josephson junction array, *Physical Review B,* 98, 6, 2018, pp. 060501-060505.

[61]. F. Loder, A. P. Kampf, T. Kopp, *et al*., Magnetic flux periodicity of h/e in superconducting loops, *Nature Physics,* 2008, 4, pp. 112-115.

Published by International Frequency Sensor Association (IFSA) Publishing, S. L., 2020 (http://www.sensorsportal.com)